frontiers | Frontiers in Physics

TYPE Original Research
PUBLISHED 12 October 2022
DOI 10.3389/fphy.2022.1027845

OPEN ACCESS

EDITED BY
Chengbo Mou,
Shanghai University, China

REVIEWED BY
Chao-qing Dai,
Zhejiang Agriculture and Forestry University, China
Li Zaidong,
Tianjin University of Science and Technology, China
Huafeng Zhang,
Huafeng Zhang,
China

*CORRESPONDENCE
Zhifang Wu,
wuzhifang01@163.com
Sijin Li,
lisjnm123@163.com

SPECIALTY SECTION
This article was submitted to Optics and Photonics,
a section of the journal
Frontiers in Physics

RECEIVED 25 August 2022
ACCEPTED 26 September 2022
PUBLISHED 12 October 2022

CITATION
Yang G, Wang S, Yuan J, Zhou H, Wu Z and Li S (2022), Oscillating propagation and parametric instability of the partial Gaussian beam in graded-index multimode fibers.
Front. Phys. 10:1027845.
doi: 10.3389/fphy.2022.1027845

Oscillating propagation and parametric instability of the partial Gaussian beam in graded-index multimode fibers

Guangye Yang[1,2], Sandan Wang[3,4], Jinpeng Yuan[3,4], Haitao Zhou[1,5,6], Zhifang Wu[1,5,6]* and Sijin Li[1,5,6]*

[1]Collaboration Innovation Center for Molecular Imaging of Precision Medicine, Shanxi Medical University, Taiyuan, China, [2]Department of Physics, Shanxi Medical University, Taiyuan, China, [3]State Key Laboratory of Quantum Optics and Quantum Optics Devices, Institute of Laser Spectroscopy, Shanxi University, Taiyuan, China, [4]Collaborative Innovation Center of Extreme Optics, Shanxi University, Taiyuan, China, [5]Department of Medical Imaging, Shanxi Medical University, Taiyuan, China, [6]Department of Nuclear Medicine, First Hospital of Shanxi Medical University, Taiyuan, China

We investigate the input and propagation characteristics and geometric parametric instability of the partial Gaussian beam limited by the fiber face area in a graded-index multimode fiber. The theoretical simulation shows that the energy of the partial Gaussian beam and the coupling efficiency of the fiber face are restricted by the fiber face area for the different powers and spot sizes of the input Gaussian beam. The spot intensity pattern of the partial Gaussian beam exhibits a standard oscillating distribution in space as the beam undergoes periodic oscillations with propagation. Also, the dynamic evolution process from parametric sidebands to a supercontinuum is affected by the peak power, the spot size of the partial Gaussian beam, and the fiber length. Finally, the experimental output spectra with different powers of the partial Gaussian beam and fiber lengths in a graded-index multimode fiber confirm the prediction of theoretical simulations. This work provides practical guidance for optimizing supercontinuum source expansion and spectral power density.

KEYWORDS

graded-index multimode fiber, partial Gaussian beam, propagation characteristics, geometric parametric instability, supercontinuum

Introduction

Multimode fibers (MMFs) have drawn renewed attention owing to their versatile platform to investigate the rich and complex phenomena in multimodal nonlinear environments such as spatiotemporal dynamics [1–3], spatial beam self-cleaning [4, 5], rogue waves [6], supercontinuum generation [7, 8], spatiotemporal mode-locking [9, 10], multimode solitons [11–13], and geometric parametric instability (GPI) [14, 15]. These studies are expected to enhance the bandwidth of telecom systems through space-division multiplexing as well as can offer a new route to mode-area scaling for high-power

lasers in imaging systems [16–18], especially oriented toward the biomedical imaging domain [19–22].

Graded-index (GRIN) MMFs play an important role in the aforementioned studies for their arbitrary deviation of the refractive index profile, so as to the mode propagation constants happen to be equidistant [23, 24]. As a result, beam revivals in the form of compressions and expansions periodically occur during propagation. Under nonlinear conditions, these natural oscillating periodic behaviors can give rise to the special class of parametric instabilities that are called GPI. Recently, GPI in GRIN-MMFs has been studied extensively from various perspectives, including the first theoretical and experimental observation [14, 15], the adjustment of sideband positions [25], the rapid replication [26], Moiré-like patterns [27], rigorous analysis [28], modal perspective [29], correlation in energy [30], and higher-order dispersion effect [31]. These reports are all basically studied by using the injected field of a Gaussian beam.

Limited by the small face of the GRIN-MMFs, the incident of a large Gaussian spot will bring the result of partial Gaussian light injection, which makes the dynamic propagation complex. The partial Gaussian beam can be represented properly by the finite superposition of the Gaussian wavelet, and the propagation of the partial Gaussian beam was calculated [32]. The analytical expression for the kurtosis parameter of partially simplified general-type beams was derived based on the second- and fourth-order moment formalism [33]. The spatially partial Gaussian pulsed beam is combined with the conventional Gaussian pulsed beam decomposition method to enable the modeling of diffraction of a general ultrashort pulse from an arbitrarily shaped hard aperture [34]. Furthermore, when the partial Gaussian beam is transmitted in the GRIN-MMFs, the energy of the beam is partially transmitted because the Gaussian beam does not enter the fiber completely and unlike the self-similar transformation pattern of the complete Gaussian beam [35]. Accordingly, the generated GPI sidebands will also be affected by the partial Gaussian beam in transmission. However, there are no reports on the propagation characteristics of partial Gaussian beams in GRIN-MMFs to the best of our knowledge.

In this study, we investigate the input and propagation characteristics and GPI of the radially symmetric partial Gaussian beam in a GRIN-MMF by employing the (3 + 1) D NLSE in theory. The restriction of the fiber face area on the Gaussian beam results in partial Gaussian beam production. Meanwhile, the spatial distributions of the partial Gaussian beam in GRIN-MMFs are observed, and it is found that it is different from the case of a Gaussian beam. Also, the generations of GPI sidebands are further studied, and the influence of the power and spot size of the partial Gaussian beam on GPI sidebands is revealed. Furthermore, the generated spectrum of the partial Gaussian beam for different input powers and fiber lengths is observed realistically and experimentally.

Theoretical model

The propagation of a spatiotemporal optical beam inside a GRIN-MMF can be theoretically described by a (3 + 1) D NLSE in the presence of a parabolic potential [14, 15].

$$i\frac{\partial\psi}{\partial z}+\frac{1}{2k_0}\nabla_\perp^2\psi+\frac{\kappa''}{2}\frac{\partial^2\psi}{\partial t^2}-\frac{k_0\Delta}{a}r^2\psi+\gamma|\psi|^2\psi=0 \qquad (1)$$

where $\psi(x,y,z,t)$ represents the complex field envelope measured in $\sqrt{W}/m$ and z and t denote the propagation distance and the retarded time in a frame of reference moving with the pulse at the group velocity v_g ($t=\tau-z/v_g$), respectively. $\nabla_\perp^2=\partial_x^2+\partial_y^2$ is the transverse Laplacian operator, $r^2=x^2+y^2$, $k_0=\omega_0 n_0/c$, n_0 is the refractive index at the center of the fiber core, Δ is the relative index difference, and a is the core radius. In addition, κ'' denotes the group-velocity dispersion evaluated at the carrier frequency ω_0, $\gamma=\omega_0 n_2/c$, and n_2 stands for the nonlinear Kerr coefficient associated with silica glass.

In general, it is assumed as an infinite parabolic profile such that the propagation constant of the modes is in equal spacing, but the highest-order modes do not have the equidistant feature arising from the effects of a cladded finite-size core. Thus, the lower-order sets of modes will remain linearly stable with periodic oscillations along the propagation [36], i.e., if a Gaussian mode beam is injected, the field remains approximately Gaussian [37]. To treat diverse practical cases, we here investigate the spatiotemporal dynamic while inputting a partial Gaussian beam in a GRIN-MMF. The analysis of nonlinear light propagation in an MMF becomes complex since it involves coupled spatial and temporal effects between hundreds or thousands of modes. From a theoretical aspect, solving the (3 + 1) D NLSE of Equation 1 is the most direct method, but it is computationally the most expensive method [11]. In this regard, several recent works have demonstrated with the neural network and deep-learning methods to improve the calculation speed [38–41]. More immediately, as suggested in [26], the (3 + 1) D problem of Eq. 1 can be approximately reduced to a (1 + 1) D NLSE through nonlinear pulse propagation. Along their lines, we take the form $\psi(x,y,z,t)=u(z,t)A(x,y,z)$ while considering continuous wave (CW) excitation. Based on perturbation schemes, we assume $u(z,t)=1+\varepsilon(z,t)$, where $\varepsilon(z,t)$ describes a small complex perturbation ($|\varepsilon|\ll 1$). For convenience, the amplitude of the background wave is taken here to be unity. By inserting the Ansatz form $\psi(x,y,z,t)$ in Eq. 1, we get

$$i\frac{\partial A}{\partial z}+\frac{1}{2k_0}\nabla_\perp^2 A-\frac{k_0\Delta}{a}r^2A+\gamma|A|^2A=0\,, \qquad (2)$$

$$i\frac{\partial\varepsilon}{\partial z}+\frac{\kappa''}{2}\frac{\partial^2\varepsilon}{\partial t^2}+\gamma\frac{\iint|A|^4dxdy}{\iint|A|^2dxdy}\left(\varepsilon+\varepsilon^*\right)=0. \qquad (3)$$

Equation 2 is used to describe the self-imaging evolution of the beam, which preserves the nonlinearity term slightly different

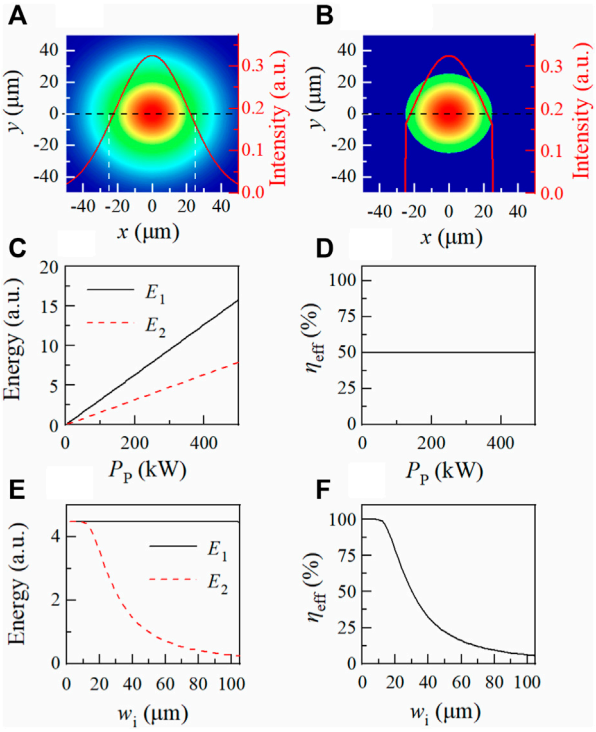

FIGURE 1
(Color inline) Spot intensity patterns before **(A)** and after **(B)** entering the fiber face with the fiber core radius $a = 25\,\mu m$ [the white dotted lines in **(A)**]. The red lines are the cross-section intensity profiles. Here, $P_p = 142$ kW, $w_i = 30\,\mu m$, and $\lambda_0 = 1064$ nm. Dependences of the energy of the complete and partial Gaussian beam E_1 and E_2, and the coupling efficiency of the fiber face η_{eff} on **(C** and **D)** the peak power P_p for a given $w_i = 30\,\mu m$ and **(E** and **F)** the spot size w_i for a given $P_P = 142$ kW.

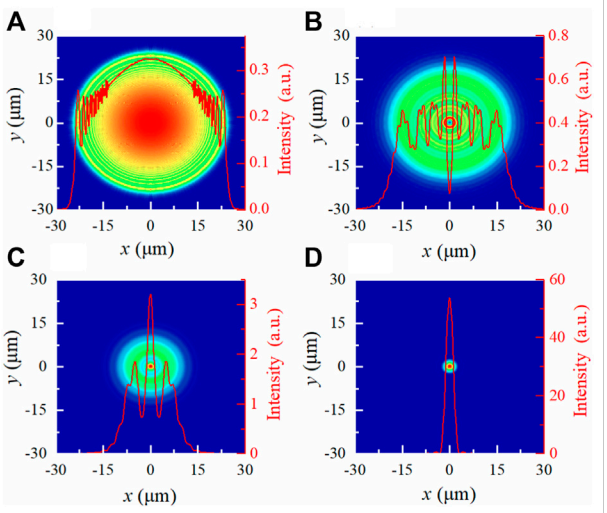

FIGURE 2
(Color inline) Evolution intensity patterns and the corresponding cross-section intensity profiles with the initial partial Gaussian beam [as shown in Figure 1B] at the distances **(A)** $z_1 = 0.007$ mm; **(B)** $z_2 = 0.091$ mm; **(C)** $z_3 = 0.183$ mm; and **(D)** $z_4 = 0.275$ mm. Here, $n_0 = 1.46$, $\Delta \approx 0.01$, and $n_2 = 1.2 \times 10^{22}\ m^2 \cdot v^{-2}$.

from [26]. Exterminating the transverse spatial dependence, Eq. 3 manages the temporal evolution of the small perturbation, which is influenced by the space field in the z-axis. If the self-imaging field is approximately linear in the aforementioned derivation, which means the absence of a nonlinearity term in Eq. 2, we can get the envelope $u(z,t)$ [26, 28]

$$i\frac{\partial u}{\partial z} + \frac{\kappa''}{2}\frac{\partial^2 u}{\partial t^2} + \gamma\frac{\iint |A|^4 dxdy}{\iint |A|^2 dxdy}|u|^2 u = 0. \quad (4)$$

Thus, Eqs. 2–4 can manage the propagation of the partial Gaussian beam and the generated GPI sidebands in a GRIN-MMF, respectively.

Input and propagation of the partial Gaussian beam

First, we assume that the input field before entering the fiber face is an on-axis Gaussian spatial beam as follows: $G(x, y, 0) = \sqrt{P_p\sigma}/w_i \exp[-r^2/(2w_i^2)]$ and $\sigma = 2\eta_0 \gamma a/(n_0\pi\sqrt{2\Delta})$, with $\eta_0 = \sqrt{\mu_0/\varepsilon_0}$, where μ_0 and ε_0 are the permeability and permittivity of the vacuum, respectively. Here, P_p is the input peak power and w_i is the beam spot size (where the intensity drops by e^{-2}). The input field after entering the fiber face is considered a radially symmetric partial Gaussian beam when the on-axis Gaussian beam spot size is larger than the fiber face. Figures 1A,B present the intensity distribution of the Gaussian beam in a transverse plane before and after entering the fiber face, respectively. It can be seen directly that the partial Gaussian beam arises from an effect of truncation on the Gaussian beam, and the distinct sharp boundary is generated as shown in Figure 1B. We define the energy of the complete Gaussian beam as $E_1 = \iint |G|^2 dxdy = \pi P_p\sigma$, the energy of the partial Gaussian beam as $E_2 = \iint_s |G|^2 dxdy = \pi P_p\sigma(1 - \exp(-a^2/w_i^2))$, where s is the area of the fiber face with the fiber radius a, and the coupling efficiency of the fiber face as $\eta_{eff} = E_2/E_1 = 1 - \exp(-a^2/w_i^2)$. Figures 1C, D show the dependences of the energies E_1, E_2 and the coupling efficiency of the fiber face η_{eff} on the initial power P_p, respectively. It can be found that for a given larger spot size w_i, the energies E_1 and E_2 are both linearly increasing (Figure 1C), and the coupling efficiency of the fiber face η_{eff} remains constant (Figure 1D), while the energy E_1 is consistent, the energy E_2 is nonlinearly decreasing and the coupling efficiency of the fiber face η_{eff} is nonlinearly decreasing (is the same trend of change with E_2) as a function of the initial spot size w_i for a given peak power P_p, which are shown in Figures 1E,F. It is to be noted that, when the spot size w_i is small, the energies E_1 and E_2 are the same and the corresponding

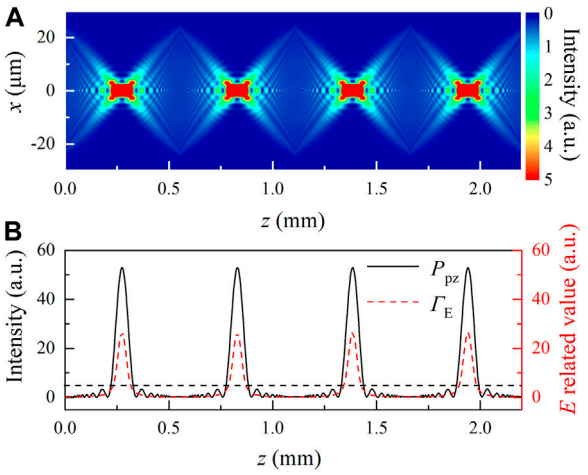

FIGURE 3
(Color inline) **(A)** Evolution of the spot cross-section intensity through a distance of 2.2 mm [the self-imaging period distance z_P = 0.55 mm]. **(B)** Evolution of the corresponding peak intensity P_{pz} and the energy-related value Γ_E. The black dotted line corresponds to the intensity value of 5. Here, the parameters are the same as in Figure 2.

coupling efficiency of the fiber face η_{eff} is a hundred percent because the complete Gaussian beam is fully coupled into the fiber.

We next analyze the evolution of the partial Gaussian beam in a GRIN-MMF. The beam evolution in an MMF is a multimodal pattern process in which principal mode propagation is a localization of a group of guided modes and Gaussian mode represents the fundamental fiber mode [42]. Under the parabolic index profile of the MMF, any stationary nonlinear mode undergoes periodic oscillations (also named the periodic self-imaging phenomenon) with a spatial period of $z_p = \pi a/\sqrt{2\Delta}$. Figure 2 shows the evolution intensity patterns and the corresponding cross-section intensity profiles with the initial partial Gaussian beam at different distances in the first half spatial period. The patterns in Figure 1B→Figure 2A–D→Figure 2D–A→Figure 1B constitute a cycle of the self-imaging process. Unlike the transformation pattern of the Gaussian beam (shown in [35]), the distribution intensity pattern of the partial Gaussian beam does not have the self-similar feature, although it is linearly stable in transmission. The distribution of the partial Gaussian beam is formed by the edge-to-center oscillation, starting at the sharp boundary, as seen in the change from Figure 1B to Figure 2A. From Figures 2B–D, one can see that the spot gradually shrinks while the oscillating distribution intensity increases as the distance increases, especially the intensity of the spot center changes alternately and finally reaches a maximum value at the distance of half a period.

We further demonstrate the periodic compressions and expansions of the partial Gaussian beam with four propagation cycles, as shown in Figure 3A. One can clearly find that the cross-section intensity profile shows a distinct oscillating distribution when the normalized intensity value is below about five. Furthermore, we can also see that the self-imaging is an approximately linear effect from Figure 3A although the nonlinearity term is preserved in Eq. 2 and the nonlinear Kerr coefficient n_2 here is larger than the ones in [15, 26]. Meanwhile, the corresponding peak intensity P_{pz} is presented in the black line of Figure 3B. It can be found that both wings of maximum peak intensities exhibit oscillatory characteristics, which indicates the alternating changes of the spot center. Through solving Eq. 2 in the presence and absence of the nonlinearity, we find that the evolutionary characteristics of the corresponding peak intensities P_{pz} in both cases are approximately uniform. Hence, we can use Eq. 4 to investigate the generated GPI sidebands in GRIN-MMFs. Physically, the periodic beam focusing enables spatial–temporal coupling, which generates a z-varying energy E-related value $\Gamma_E(Z) = (\iint|A(x,y,z)|^4 dxdy)/(\iint|A(x,y,z)|^2 dxdy)$. Also, it couples the spatial evolution to the temporal envelope, resulting in the periodic Kerr nonlinearity [the last term of Eq. 4]. By numerically calculating the ratio of the two overlaps that integrate over the z-varying transverse plane of the partial Gaussian beam, one can get that the evolution plots of the related value $\Gamma_E = P_{pz}/2$ as shown in Figure 3B with a red dotted line.

The generated GPI sidebands

We next analyze the GPI sidebands in the GRIN-MMF, which play a prominent role in inciting supercontinuum generation. The GPI sidebands at different distances for two peak powers are obtained by solving Eq. 4 with a CW excitation, as shown in Figures 4A,B. One can see that for the case of high peak power, GPI first generates a series of narrow spectral sidebands, which then gradually broaden accompanying the increased intensity and eventually evolve into a supercontinuum. For the low peak power case, the GPI sidebands have the same evolutionary trend but at a slower rate. It is concluded that the spectrum is favorable to be broadened with higher peak power because of the enhanced self-phase modulation and four-wave mixing effects. It is worth noting that the frequency detuning of each sideband center $f_1, f_2, f_3, \ldots$ has a small shift for two different peak powers.

We further consider the dependence of the intensity and the frequency detuning of the sideband center f_1 and f_2 on the peak power P_p and the spot size w_i, respectively. It can be seen that the intensities of f_1 and f_2 are linearly increasing and the frequency detuning is linearly decreasing as a function of the peak power P_p from Figures 5A,B, respectively. Conversely, the intensities are nonlinearly decreasing and the frequency detuning is nonlinearly increasing as a function of the spot size w_i, as shown in Figures

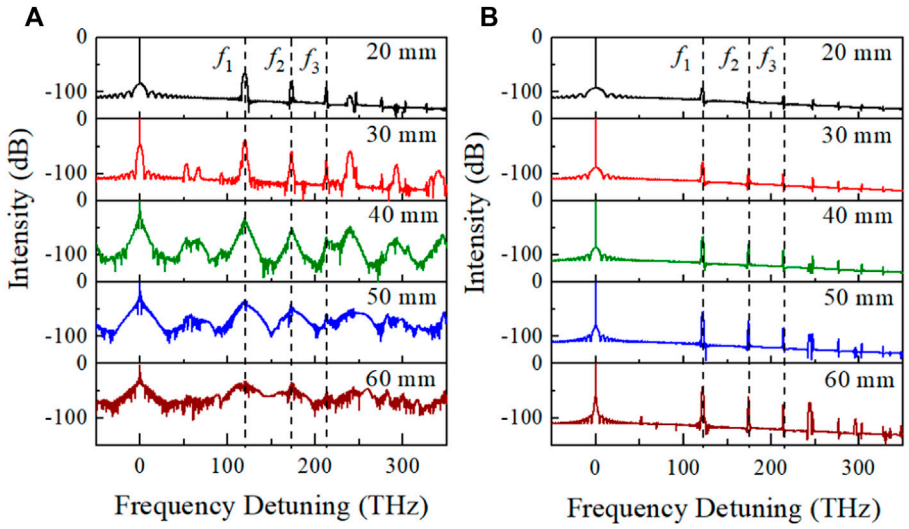

FIGURE 4
(Color online) Spectrum profile at different distances excited by the partial Gaussian beam with the peak power **(A)** P_p = 300 kW and **(B)** P_p = 142 kW when spot size w_i = 30μm. The frequency detuning of the first, second, and third sideband centers f_1, f_2, and f_3 is delineated with the black dotted lines, respectively. Here, κ'' = 1.75 s^{-26}/m, and the other parameters are the same as in Figure 2.

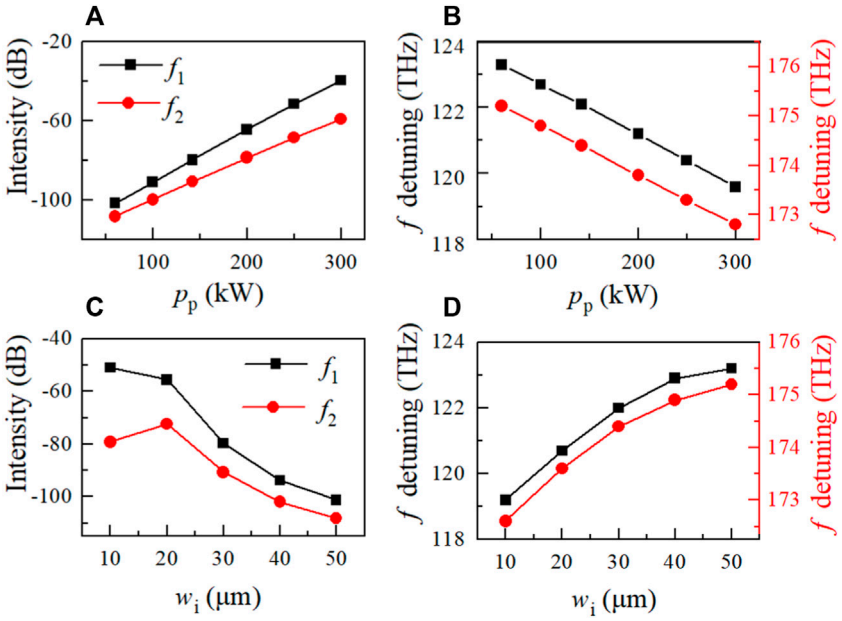

FIGURE 5
(Color online) Dependences of the intensity and frequency detuning of the first and second sideband center f_1 and f_2 at a distance z = 30 *mm* on **(A** and **B)** the peak power P_p with w_i = 30 μm and **(C** and **D)** the spot size w_i with P_P = 142 kW. Here, the other parameters are the same as in Figure 4.

5C,D, respectively. Those results indicate that the supercontinuum generation and the frequency tendency from GPI sidebands to the pump source are more favorable with increased peak power and decreased spot size. Similar results of frequency shift and supercontinuum generation in GPI sidebands with the increasing fiber core radius were also found in [25].

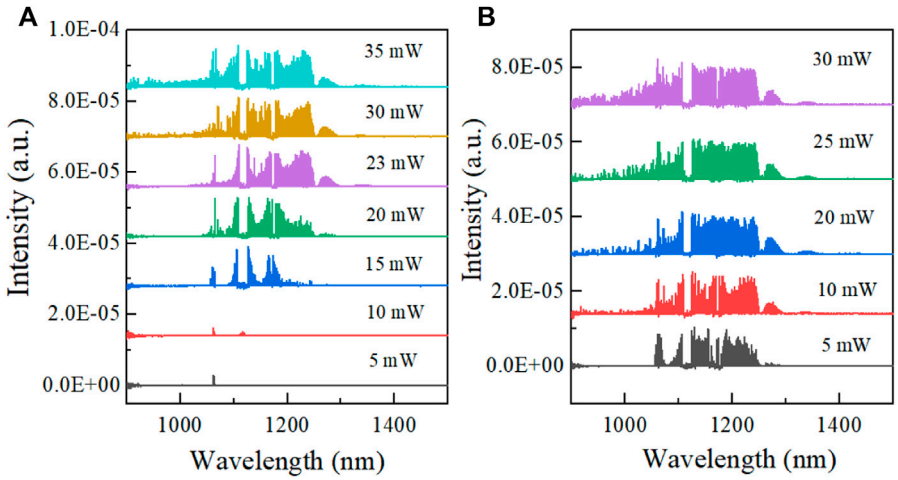

FIGURE 6
(Color online) Output spectra obtained from the **(A)** 30-m GRIN-MMF with 40% coupling efficiency and **(B)** 10-m GRIN-MMF with 60% coupling efficiency at different average powers.

Experimental observation of the frequency spectrum

In the experiment, an amplified Q-switched microchip laser is used as a pump source, which delivers 94 μJ pulses at 1,064 nm with a pulse duration of 400 ps and a repetition rate of 500 Hz. The linearly polarized Gaussian pump pulses are launched into the GRIN-MMF with a core diameter of 50 μm, NA = 0.200, and a refractive index contrast of 1.482 (Thorlabs, GIF50C). Three lenses with focal lengths of 50 mm, 50 mm, and 70 mm are used for beam focusing. At the input face of the fiber, the beam has a diameter of 200 μm, which is greater than the fiber core diameter. A large set of transverse spatial modes is excited at the fiber input by focusing the laser beam. Also, the output beam from the GRIN-MMF is detected by using an optical spectrum analyzer covering the spectral range from 600 to 1700 nm (Yokogawa, AQ6370C).

The experimentally observed spectra for different average powers and fiber lengths are shown in Figure 6. In the case of Figure 6A, the 400-ps pump pulse at 1,064 nm is launched into a 30-m GRIN-MMF, which has a free space coupling efficiency of 40%. It can be found that the pump pulse experiences tiny spectral broadening for relatively low average power (5 and 10 mW). Further spectral broadening is observed with the increasing average power. When the average power reaches 35 mW, no more obvious spectral broadening occurred. Similarly, in the case of Figure 6B, the pump pulse is launched into a 10-m GRIN-MMF with 60% free space coupling efficiency. It can be found that spectral broadening can be observed at a low average power. Meanwhile, the spectrum is further broadened with the increasing average power. The experimental results confirm the numerical simulation results of the influence of peak power on the spectral broadening as shown in Figure 4. The influence of the fiber length on spectrum broadening is not observed because the coupling efficiency of the 30-m fiber is lower than that of the 10-m fiber.

Conclusion

In summary, we numerically explore the input and propagation characteristics and GPI sidebands of the partial Gaussian beam in GRIN-MMFs. The energy dependences of the complete and partial Gaussian beams and the coupling efficiency on the peak power and the spot size are shown, respectively. The partial Gaussian beam with a sharp boundary presents the spatial distribution of oscillation in propagation. Our studies indicate that each GPI sideband gradually strengthened and broadened with the increasing fiber length and finally formed a supercontinuum. Also, the intensity and frequency detuning of the sideband center frequency depend on the peak power and the spot size. Meanwhile, the generated supercontinuum spectra of the partial Gaussian beam in GRIN-MMFs are observed experimentally. Our studies provide actual operation guidance for optimizing the spectral extent and spectral power density of supercontinuum sources based on the GPI in GRIN-MMFs.

Data availability statement

The original contributions presented in the study are included in the article/supplementary material; further inquiries can be directed to the corresponding authors.

Author contributions

GY was the main author and responsible for the first draft of the manuscript. All authors provided reviews and comments on subsequent versions of the manuscript. GY, JY, and ZW conceived the idea. GY performed the numerical simulations. SW and JY performed the experiments. HZ conducted the data processing. GY, JY, ZW, and SL provided support with the setup, analysis, and interpretation of results.

Funding

The authors acknowledge support from the National Natural Science Foundation of China (Grant Nos. 61505101, 62005150, 82027804, 81971655, and 82102103), the Natural Science Foundation of Shanxi province (No. 201901D111212), and the Shanxi Scholarship Council of China (No. 2020-073).

Acknowledgments

The authors thank Fan O. Wu for fruitful discussions on the MMF theory. They also thank Helena E. Lopez Aviles for her help with the simulations.

Conflict of interest

The authors declare that the research was conducted in the absence of any commercial or financial relationships that could be construed as a potential conflict of interest.

Publisher's note

References

1. Wright LG, Christodoulides DN, Wise FW. Controllable spatiotemporal nonlinear effects in multimode fibres. *Nat Photon* (2015) 9:306–10. doi:10.1038/nphoton.2015.61

2. Picozzi A, Millot G, Wabnitz S. Nonlinear virtues of multimode fibre. *Nat Photon* (2015) 9:289–91. doi:10.1038/nphoton.2015.67

3. Wabnitz S, Krupa K, Couderc V, Modotto D, Barthélémy A, Millot G, et al. Nonlinear dynamics in multimode optical fibers. *Proc SPIE* (2018) 10540:105402B. doi:10.1117/12.2287874

4. Krupa K, Tonello A, Shalaby BM, Fabert M, Barthélémy A, Millot G, et al. Spatial beam self-cleaning in multimode fibres. *Nat Photon* (2017) 11:237–41. doi:10.1038/nphoton.2017.32

5. Liu Z, Wright LG, Christodoulides DN, Wise FW. Kerr self-cleaning of femtosecond-pulsed beams in graded-index multimode fiber. *Opt Lett* (2016) 41:3675–8. doi:10.1364/ol.41.003675

6. Dudley JM, Dias F, Erkintalo M, Genty G. Instabilities, breathers and rogue waves in optics. *Nat Photon* (2014) 8(10):755–64. doi:10.1038/nphoton.2014.220

7. Lopez-Galmiche G, Eznaveh ZS, Eftekhar MA, Lopez JA, Wright LG, Wise F, et al. Visible supercontinuum generation in a graded index multimode fiber pumped at 1064 nm. *Opt Lett* (2016) 41:2553–6. doi:10.1364/ol.41.002553

8. Krupa K, Louot C, Couderc V, Fabert M, Guenard R, Shalaby BM, et al. Spatiotemporal characterization of supercontinuum extending from the visible to the mid-infraredin a multimode graded-index optical fiber. *Opt Lett* (2016) 41:5785–8. doi:10.1364/ol.41.005785

9. Guenard R, Krupa K, Dupiol R, Fabert M, Bendahmane A, Kermene V, et al. Nonlinear beam self-cleaning in a coupled cavity composite laser based on multimode fiber. *Opt Express* (2017) 25:22219–27. doi:10.1364/oe.25.022219

10. Wright LG, Christodoulides DN, Wise FW. Spatiotemporal mode-locking in multimode fiber lasers. *Science* (2017) 358:94–7. doi:10.1126/science.aao0831

11. Renninger WH, Wise FW. Optical solitons in graded-index multimode fibres. *Nat Commun* (2013) 4:1719. doi:10.1038/ncomms2739

12. Ahsan AS, Agrawal GP. Graded-index solitons in multimode fibers. *Opt Lett* (2018) 43(14):3345–8. doi:10.1364/OL.43.003345

13. Sun YF, Zitelli M, Ferraro M, Mangini F, Parra-Rivas P, Wabnitz S. Multimode soliton collisions in graded-index optical fibers. *Opt Express* (2022) 30:21710–4. doi:10.1364/OE.459447

14. Longhi S. Modulational instability and space time dynamics in nonlinear parabolic-index optical fibers. *Opt Lett* (2003) 28:2363–5. doi:10.1364/ol.28.002363

15. Krupa K, Tonello A, Barthélémy A, Couderc V, Shalaby BM, Bendahmane A, et al. Observation of geometric parametric instability induced by the periodic spatial self-imaging of multimode waves. *Phys Rev Lett* (2016) 116:183901. doi:10.1103/physrevlett.116.183901

16. Richardson DJ, Fini JM, Nelson LE. Space-division multiplexing in optical fibres. *Nat Photon* (2013) 7:354–62. doi:10.1038/nphoton.2013.94

17. Wright LG, Wabnitz SW, Christodoulides DN, Wise FW. Ultrabroadband dispersive radiation by spatiotemporal oscillation of multimode waves. *Phys Rev Lett* (2015) 115:223902. doi:10.1103/physrevlett.115.223902

18. Krupa K, Tonello A, Barthélémy A, Mansuryan T, Couderc V, Millot G, et al. Multimode nonlinear fiber optics, a spatiotemporal avenue. *APL Photon* (2019) 4(11):110901. doi:10.1063/1.5119434

19. Seddon AB, Napier B, Lindsay I, Lamrini S, Moselund PM, Stone N, et al. Prospective on using fibre mid-infrared supercontinuum laser sources for *in vivo* spectral discrimination of disease. *Analyst* (2018) 143:5874–87. doi:10.1039/c8an01396a

20. Zhang Y, Cao Y, Cheng JX. High-resolution photoacoustic endoscope through beam self-cleaning in a graded index fiber. *Opt Lett* (2019) 44(19):3841–4. doi:10.1364/ol.44.003841

21. Teng ZS, Gao F, Xia H, Chen WL, Li CX. *In vivo* pulse wave measurement through a multimode fiber diffuse speckle analysis system. *Front Phys* (2020) 8:613342. doi:10.3389/fphy.2020.613342

22. Wehbi S, Mansuryan T, Krupa K, Fabert M, Tonello A, Zitelli M, et al. Continuous spatial self-cleaning in GRIN multimode fiber for self-referenced multiplex CARS imaging. *Opt Express* (2022) 29:16104–14. doi:10.1364/oe.452384

23. Meunier JP, Pigeon J, Massot JN. Analyse perturbative des caractéristiques de propagation des fibres optiques à gradientd' indice quasi-parabolique. *Opt Quan Electron* (1980) 12:41–9. doi:10.1007/bf00625497

24. Sammut RA, Ghatak AK. Perturbation theory of optical fibres with power-law core profile. *Opt Quan Electron* (1978) 10:475–82. doi:10.1007/bf00619848

25. Eznaveh ZS, Eftekhar MA, Lopez JEA, Kolesik M, Schlzgen A, Wise FW, et al. Tailoring frequency generation in uniform and concatenated multimode fibers. *Opt Lett* (2017) 42:1015–8. doi:10.1364/ol.42.001015

26. Conforti M, Arabi CM, Mussot A, Kudlinski A. Fast and accurate modeling of nonlinear pulse propagation in graded-index multimode fibers. *Opt Lett* (2017) 42(19):4004–7. doi:10.1364/ol.42.004004

27. Mas Arabí C, Kudlinski A, Mussot A, Conforti M. Geometric parametric instability in periodically modulated graded-index multimode fibers. *Phys Rev A (Coll Park)* (2018) 97(2):023803. doi:10.1103/physreva.97.023803

28. Lopez-Aviles HE, Wu FO, Sanjabi Eznaveh Z, Eftekhar MA, Wise F, Amezcua Correa R, et al. A systematic analysis of parametric instabilities in nonlinear parabolic multimode fibers. *APL Photon* (2019) 4(2):022803. doi:10.1063/1.5044659

29. He W, Dai J, Ma Q, Luo A, Hong W. Modal perspective on geometric parametric instability sidebands in graded-index multimode fibers. *Opt Express* (2021) 29:11353–60. doi:10.1364/oe.422667

30. Deng Z, Chen Y, Liu J, Zhao C, Fan D. Correlation between geometric parametric instability sidebands in graded-index multimode fibers. *Chaos* (2021) 31(1):013109. doi:10.1063/5.0028713

31. Bendahmane A, Conforti M, Vanvincq O, Arabi CM, Mussot A, Kudlinski A. Origin of spontaneous wave mixing processes in multimode GRIN fibers. *Opt Express* (2021) 29:30822–33. doi:10.1364/oe.436229

32. Cywiak M, Cywiak D, Yáñez E. Finite Gaussian wavelet superposition and Fresnel diffraction integral for calculating the propagation of truncated, non-diffracting and accelerating beams. *Opt Commun* (2017) 405:132–42. doi:10.1016/j.optcom.2017.08.015

33. Ouahid L, Nebdi H, Dalil-Essakali L. Kurtosis factor of truncated and non-truncated simplified general-type beams. *Opt Quan Electron* (2017) 49:91. doi:10.1007/s11082-017-0934-6

34. Worku NG, Gross H. Spatially truncated Gaussian pulsed beam and its application in modeling diffraction of ultrashort pulses from hard apertures. *J Opt Soc Am A* (2020) 37:317–26. doi:10.1364/josaa.382133

35. Deng ZX, Chen Y, Liu J, Zhao CJ, Fan DY. Emission of multiple resonant radiations by spatiotemporal oscillation of multimode dark pulses. *Opt Express* (2019) 27:36022–33. doi:10.1364/oe.27.036022

36. Longhi S, Janner D. Self-focusing and nonlinear periodic beams in parabolic index optical fibres. *J Opt B: Quan Semiclass Opt* (2004) 6:S303–8. doi:10.1088/1464-4266/6/5/019

37. Karlsson M, Anderson D, Desaix M. Dynamics of self-focusing and self-phase modulation in a parabolic index optical fiber. *Opt Lett* (1992) 17:22–4. doi:10.1364/ol.17.000022

38. Salmela L, Tsipinakis N, Foi A, Billet C, Dudley JM, Genty G. Predicting ultrafast nonlinear dynamics in fibre optics with a recurrent neural network. *Nat Mach Intell* (2021) 3:344–54. doi:10.1038/s42256-021-00297-z

39. Teğin U, Dinç NU, Moser C, Psaltis D. Reusability report: Predicting spatiotemporal nonlinear dynamics in multimode fibre optics with a recurrent neural network. *Nat Mach Intell* (2021) 3:387–91. doi:10.1038/s42256-021-00347-6

40. Wen XK, Wu GZ, Liu W, Dai CQ. Dynamics of diverse data-driven solitons for the three-component coupled nonlinear Schrödinger model by the MPS-PINN method. *Nonlinear Dyn* (2022) 109:3041–50. doi:10.1007/s11071-022-07583-4

41. Fang Y, Wu GZ, Wen XK, Wang YY, Dai CQ. Predicting certain vector optical solitons via the conservation-law deep-learning method. *Opt Laser Technol* (2022) 155:108428. doi:10.1016/j.optlastec.2022.108428

42. Nolan DA, Nguyen DT. Light localization and principal mode propagation in optical fibers. *Front Phys* (2021) 9:713085. doi:10.3389/fphy.2021.713085